

pubs.acs.org/JPCA Article

Charge Migration in HCCI Cations Probed by Strong Field Ionization: Time-Dependent Configuration Interaction and Vibrational Wavepacket Simulations

Published as part of The Journal of Physical Chemistry A virtual special issue "Krishnan Raghavachari Festschrift".

H. Bernhard Schlegel*



Cite This: J. Phys. Chem. A 2023, 127, 6040-6050

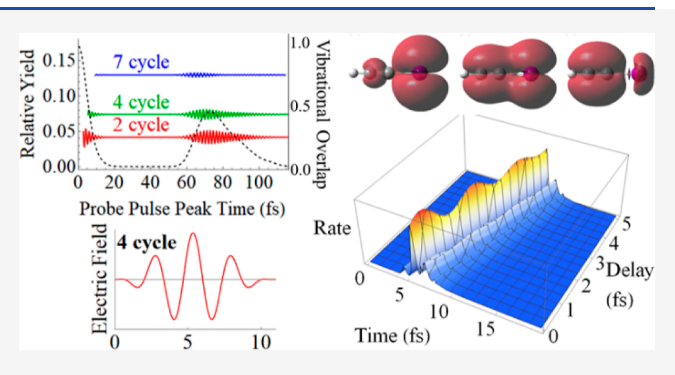


ACCESS

Metrics & More

Article Recommendations

ABSTRACT: Strong field ionization of neutral iodoacetylene (HCCI) can produce a coherent superposition of the X and A cations and results in charge migration between the CC π orbital and the iodine π -type lone pair. This charge migration causes oscillations in the rate of strong field ionization of the cation to the dication that can be monitored using intense few-cycle probe pulses. The dynamics and strong field ionization of the coherent superposition the X and A states of HCCI⁺ have been modeled by time-dependent configuration interaction (TDCI) simulations. When the nuclei are allowed to move, the electronic wavefunctions need to be multiplied by vibrational wavefunctions. Nuclear motion has been modeled by vibrational packets moving on quadratic



approximations to the potential energy surfaces for the X and A states of the cation. The overlap of the vibrational wavepackets decays in about 10–15 fs. Consequently, the oscillations in the strong field ionization decay on the same time scale. A revival of the vibrational overlap and in the oscillations of the strong field ionization is seen at 60–110 fs. TDCI simulations show that the decay and revival of the charge migration can be monitored by strong field ionization with intense 2- and 4-cycle linearly polarized 800 nm pulses. The revival is also seen with 7-cycle pulses.

■ INTRODUCTION

Charge migration can be produced by a coherent superposition of electronic states. Such electronic dynamics have been observed in a few atomic and molecular systems on time scales of a few femtoseconds to tens of femtoseconds. 1-5 Attosecond transient absorption, attosecond pump-IR probe, high harmonic spectroscopy, and attosecond streaking are able to achieve the temporal resolution needed to observe these effects. 1-8 Strong field ionization can be used to produce coherent superpositions of cation states. Potentially, strong field ionization can also be used to probe the charge migration resulting from the coherent superposition. Iodoacetylene (HCCI) has been chosen as a test case because the dynamics of the cations of HCCI have been studied extensively by both experimental and theoretical methods. 4,9-13 The coherent superposition of the X and A states of HCCI+ leads to charge migration between the C \equiv C π orbital and the iodine π -type lone pair. Based on higher harmonic spectroscopy and theoretical simulations of electron dynamics, Kraus et al. were able to reconstruct both the amplitude and relative phase of the superposition of the X and A states of HCCI⁺ and the resulting charge migration. Yang et al. included

both electronic and nuclear dynamics in their simulation of the superposition of the X and A states of HCCI $^+$ and found decoherence and recoherence of charge migration as a result of nuclear motion. $^{11-13}$ In earlier simulations on H_2^+ , Bandrauk and co-workers showed that charge migration and decoherence could be monitors by photoionization. 14,15 In the present study, we employ simulations of electronic and nuclear dynamics to test whether strong field ionization can be used to directly observe charge migration in HCCI $^+$.

Theoretical and computational methods for describing electron dynamics and ionization in strong laser fields have been discussed in a number of recent reviews. ^{16–21} Accurate solutions for the time-dependent Schrodinger equation are practical only for one- and two-electron systems. The single

Received: April 23, 2023 Revised: June 17, 2023 Published: July 17, 2023





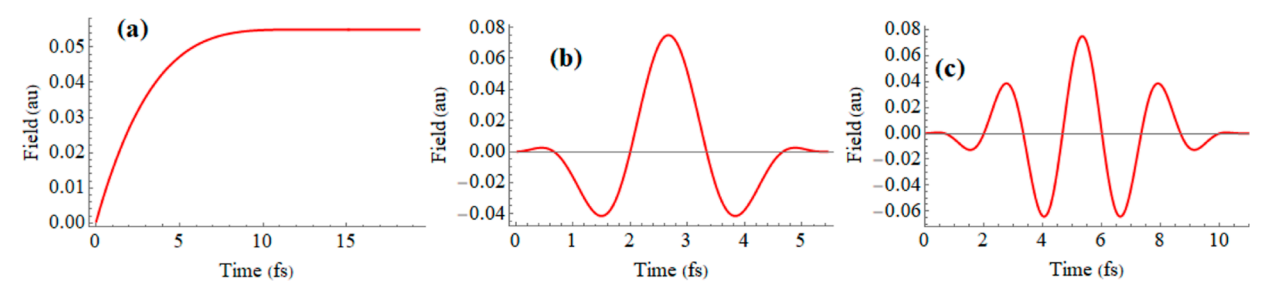


Figure 1. Electric field of (a) a "static" pulse, (b) 2-cycle linearly polarized pulse with CEP = 0, and (c) a 4-cycle linearly polarized pulse with CEP = 0.

active electron approximation and the strong field approximation are often used for multi-electron systems. Molecular Ammosov–Delone–Krainov²² and weak-field asymptotic theory²³ can model orientation-dependent ionization rates. More detailed descriptions require numerical simulations of the electron dynamics (for recent reviews, see refs 18–21). Realtime integration of time-dependent density functional theory^{24–30} and time-dependent configuration interaction^{31–38} (TDCI) have been used successfully to simulate strong field ionization for multi-electron polyatomic systems. In these approaches, a complex absorbing potential (CAP) is used to remove the outgoing electron density to model strong field ionization.

Treating nuclear dynamics is an essential part of modeling charge migration and decoherence (for recent perspectives, see refs 39 and 40). The states involved in the coherent superposition may have significantly different potential energy surfaces leading to different dynamics for the vibrational wavepackets on these surfaces. The most accurate method for calculating the vibrational dynamics is multi-configuration timedependent Hartree, 41,42 but this requires fitted potential energy surfaces and grows exponentially with the number of degrees of freedom. Alternatively, the potential energy surfaces can be calculated on-the-fly and coupled with a fully quantum treatment of the vibrations in methods such as variational multiconfigurational Gaussian, 43,44 ab initio multiple spawning, 45 multi-configurational Ehrenfest, 46,47 etc. More approximate approaches include semiclassical methods that propagate frozen or thawed Gaussian wavepackets on-the-fly. 48-50 Instead of obtaining fitted potential energy surfaces or calculating them onthe-fly, the potential energy surfaces can be represented by local quadratic approximations, provided there are no complications such as surface crossings, double wells, or large anharmonicities. Arnold, Vendrell, and Santra have found this approach satisfactory for modeling decoherence in water, paraxylene, and phenylalanine. ^{51,52} Yang and co-workers ^{11–13} examined this approach in detail for the nuclear dynamics of a coherent superposition of the X and A states of iodoacetylene cation and successfully modeled the decoherence of charge migration.

In earlier works, we employed TDCI with a CAP to study the angular dependence of strong field ionization. ^{37,38,53–60} Recently, we have used TDCI to study the coherent superposition of the X and A states of HCCI⁺. ⁶⁰ The focus of the study was on strong field ionization to probe the electron dynamics and charge migration in HCCI⁺. To avoid the effects of decoherence caused by nuclear motion during the pulse, the probe pulses were limited to two cycles. The present study includes nuclear dynamics in order to examine the impact of decoherence on strong field ionization as a probe for charge migration in HCCI⁺. The results are in excellent agreement with the findings of Yang and co-workers ^{11–13} on the effect of nuclear dynamics on the

time-scale for decoherence and recoherence in the electron flux in the coherent superposition of the X and A states of HCCI⁺. The present study shows that the decay of the charge migration can be monitored by strong field ionization with intense 2 and 4-cycle linearly polarized 800 nm pulses and that the revival of charge migration can be seen with 2, 4, and 7-cycle pulses.

METHODS

In the TDCI approach, the electronic wavefunction is propagated with the time-dependent Schrödinger equation including a CAP.

$$i\hbar \frac{\partial}{\partial t} \Psi^{\text{el}}(t) = \hat{\mathbf{H}}(t) \Psi^{\text{el}}(t) = [\hat{\mathbf{H}}_{\text{el}} - \hat{\vec{\mu}} \cdot \vec{E}(t) - i\hat{\mathbf{V}}^{\text{abs}}] \Psi^{\text{el}}(t)$$
(1)

 $\hat{\mathbf{H}}_{\mathrm{el}}$ is the field-free, time-independent electronic Hamiltonian and $\hat{\mathbf{V}}^{\mathrm{abs}}$ is the CAP. The absorbing potential for the molecule is constructed from spherical potentials centered on each atom and is equal to the minimum of the values of the atomic absorbing potentials.³⁷ Each spherical atomic absorbing potential rises quadratically starting at R_{A} and turns over quadratically to a constant value of V_{max} beyond R_{B} .

$$\begin{split} V &= 2V_{\text{max}}[(R-R_{\text{A}})/(R_{\text{B}}-R_{\text{A}})]^{2}, \\ R_{\text{A}} &\leq R \leq (R_{\text{A}}+R_{\text{B}})/2 \\ V &= V_{\text{max}} - 2V_{\text{max}}[(R-R_{\text{A}})/(R_{\text{B}}-R_{\text{A}})]^{2}, \\ (R_{\text{A}}+R_{\text{B}})/2 &\leq R \leq R_{\text{B}} \\ V &= 0, \qquad R \leq R_{\text{A}} \text{ and } V = V_{\text{max}}, \qquad R \geq R_{\text{B}} \end{split} \tag{2}$$

The interaction with the electric field of an intense laser pulse is treated in the semiclassical dipole approximation, where $\hat{\vec{\mu}}$ is the dipole operator and \vec{E} is the electric field (see Figure 1). The electric field for an n cycle linearly polarized pulse with a \sin^2 envelope can be written as

$$E_x(t) = E_{\text{max}} \sin(\omega t/2n)^2 \cos(\omega t - \phi)$$
 for $0 \le \omega t \le 2n\pi$, $E(t) = 0$ for $\omega t \ge 2n\pi$

where ω is the angular frequency and ϕ is the carrier envelope phase (CEP).

In the TDCI approach, the wavefunction is written as a linear combination of time-dependent coefficients with time-independent configurations.

$$\Psi^{\text{el}}(t) = \sum_{i} c_{i}(t)\psi_{i} \tag{4}$$

The ψ_i are chosen as the eigenfunctions of the time-independent, field-free electronic Hamiltonian; hence, $\mathbf{H}_{\rm el} = \langle \psi | \hat{\mathbf{H}}_{\rm el} | \psi \rangle$ is a diagonal matrix. In this approach, the time-dependent Schrödinger equation for the time-dependent coefficients becomes a set of linear differential equations. The propagation of the coefficients can be written in terms of an exponential of the Hamiltonian matrix (shown in atomic units, $\hbar = 1$).

$$i\frac{\partial}{\partial t}\mathbf{c}(t) = \mathbf{H}(t)\mathbf{c}(t); \qquad H_{ij}(t) = \langle \psi_i | \hat{\mathbf{H}}(t) | \psi_j \rangle$$
$$\mathbf{c}(t + \Delta t) = \exp(-i\mathbf{H}(t)\Delta t)\mathbf{c}(t)$$
(5)

For a linearly polarized pulse (eq 3), the Trotter factorization of the exponential of the full Hamiltonian matrix is

$$\mathbf{c}(t + \Delta t) = \exp(-i\mathbf{H}_{el}\Delta t/2) \exp(-\mathbf{V}^{abs}\Delta t/2)$$

$$\times \mathbf{W}^{T} \exp(iE_{2}(t + \Delta t/2) \mathbf{d}\Delta t)\mathbf{W}$$

$$\times \exp(-\mathbf{V}^{abs}\Delta t/2) \exp(-i\mathbf{H}_{el}\Delta t/2)\mathbf{c}(t)$$
(6)

where $\mathbf{W}\mathbf{D}\mathbf{W}^{\mathrm{T}} = \mathbf{d}$ are the eigenvalues and eigenvectors of the transition dipole matrix \mathbf{D} . The exponential of $\mathbf{V}^{\mathrm{abs}}$, the eigenvectors of field-free electronic Hamiltonian and the transition dipole matrix and the product $\exp\left(-\mathbf{V}^{\mathrm{abs}}\Delta t/2\right)\mathbf{W}^{\mathrm{T}}$ need to be calculated only once since they are time-independent; $\exp\left(-i\mathbf{H}_{\mathrm{el}}\Delta t/2\right)$ and $\exp\left(iE(t+\Delta t/2)\mathbf{d}\Delta t\right)$ are easily calculated because \mathbf{H}_{el} and \mathbf{d} are diagonal matrices. A propagation step for a linearly polarized pulse involves two full matrix—vector multiples and three diagonal matrix—vector multiples. ⁵³

In simulations of strong field ionization with TDCI, the oscillating field excites an electron to high-lying states where the electron interacts strongly with $\hat{\mathbf{V}}^{abs}$ and is absorbed. For single ionization of a neutral molecule to a cation, a spin-restricted wavefunction consisting of the ground state and all singly excited configurations (CIS) is suitable. For ionization of a cation to a dication, a spin-unrestricted wavefunction could be used, but this treats the α and β spin-orbitals differently (for a linear π cation, the π_x and π_y orbitals would also be different). This problem can be overcome by using a CISD-IP wavefunction.⁶¹ The wavefunction is constructed using the molecular orbitals of the closed shell system and includes singly ionized determinants, ψ_{x} and singly excited, singly ionized determinants, ψ_{xi}^a thereby treating the α and β spin-orbitals equivalently (likewise, π_x and π_y orbitals for linear molecules are treated equivalent). The CISD-IP wavefunction used in simulations of ionization of a cation to a

$$\Psi^{\mathrm{el}}(t) = \sum_{x} c_{x} \psi_{x} + \sum_{\overline{x}} c_{\overline{x}} \psi_{\overline{x}} + \sum_{iax} c_{ix}^{a} \psi_{ix}^{a} + \sum_{ia\overline{x}} c_{i\overline{x}}^{a} \psi_{i\overline{x}}^{a} + \sum_{\overline{i}a\overline{x}} c_{\overline{i}\overline{x}}^{\overline{a}} \psi_{\overline{i}\overline{x}}^{\overline{a}} + \sum_{\overline{i}a\overline{x}} c_{\overline{i}\overline{x}}^{\overline{a}} \psi_{\overline{i}\overline{x}}^{\overline{a}}$$

$$(7)$$

where x are the ionized molecular orbitals (i < x when i and x are the same spin).⁵⁹

The ionization rate can be calculated as the rate of decrease of the norm squared of the electronic wavefunction, $\langle \Psi(t)|\Psi(t)\rangle$, which is proportional to the integral over the absorbing potential.

rate
$$(t) = -\partial \langle \Psi(t) | \Psi(t) \rangle / \partial t = 2 \langle \Psi(t) | \mathbf{V}^{abs} | \Psi(t) \rangle$$
 (8)

When nuclear dynamics is included, the total wavefunction has contributions from electronic and vibrational components. If

cations are obtained by ionization of a neutral molecule, the potential energy surfaces for the cations can differ significantly from the neutral, and the cations may have considerable vibrational energy. In the Born—Huang expansion, the molecular wavefunction is written as an electronic wavefunction that depends on the electron coordinates, \mathbf{r} , and parametrically on the nuclear coordinates, \mathbf{R} , times a vibrational wavefunction that depends only on the molecular coordinates, \mathbf{R} .

$$\Psi(\mathbf{r}, \mathbf{R}) = \Psi^{el}(\mathbf{r}; \mathbf{R})\Phi^{vib}(\mathbf{R})$$
(9)

The total ionization rate depends on the rates for the individual states and on the interaction between them, weighted by the coefficients of the electronic states and by the vibrational wavefunctions for those states.

rate
$$(t) = 2\langle \Psi(t)|\mathbf{V}^{\text{abs}}|\Psi(t)\rangle$$

$$= 2\sum_{istate,jstate}^{Nstates} c_{istate}^{\text{el}*}(t)c_{jstate}^{\text{el}}(t)\langle \Psi_{istate}^{\text{el}}|\mathbf{V}^{\text{abs}}|\Psi_{jstate}^{\text{el}}\rangle$$

$$\langle \Phi^{\text{vib},istate}(\mathbf{R},t)|\Phi^{\text{vib},jstate}(\mathbf{R},t)\rangle$$
(10)

The vibrational part of the wavefunction for a given electronic state can be approximated by a product of normal mode vibrations. In turn, a wavepacket for a single normal mode can be written as a linear combination of harmonic oscillators, $\chi_{v}^{ivib,istate}(q_{ivib})$, for mode ivib of state istate and with vibrational quantum numbers v. The harmonic oscillator functions for a given state are centered on the minimum energy geometry for that state. The displacement of the minimum for a mode of a cation state relative the neutral ground state is obtained by projecting the change in the geometry onto that normal mode. As in previous applications, $^{11-13,51,52}$ the present form assumes that the cations have the same normal modes as the ground state and that there is no intermode coupling of the vibrations in the cation states.

$$\Phi^{istate}(\mathbf{R}, t) = \prod_{\substack{ivib \\ ivib, istate}}^{\text{normal modes vibrational quanta}} \sum_{\nu}^{civib, istate}(t)$$

$$\chi_{\nu}^{ivib, istate}(q_{ivib}) \tag{11}$$

The coefficients in the vibrational wavefunction are time-dependent. Since the laser pulse used for strong field ionization (e.g., 800 nm) couples only weakly to the vibrational motions, the time dependence of the vibrational coefficients is simply a phase factor that depends on the energy.

$$c_{\nu}^{ivib,istate}(t) = c_{\nu}^{ivib,istate} e^{-iE_{\nu}^{ivib,istate}t}$$
(12)

In the Franck–Condon approximation, the initial vibrational coefficients, $c_{\nu}^{ivib,istate}$, are obtained from the overlap of the excited state vibrational wavefunctions with the zero-point vibrational wavefunction of the ground state. The time-dependent overlap of the vibrational wavepackets for states *istate* and *jstate* of the cation is given by

$$\begin{split} \langle \Phi^{\text{vib},istate}(t)|\Phi^{\text{vib},jstate}(t)\rangle \\ &= \prod_{ivib} \sum_{v,v'} c_v^{ivib,istate} * c_{v'}^{ivib,jstate} \\ &= \exp(i(E_v^{ivib,istate} - E_{v'}^{ivib,jstate})t) \\ &\langle \chi_v^{ivib,istate}(q_{ivib})|\chi_v^{ivib,jstate}(q_{ivib})\rangle \end{split} \tag{13}$$

The overlap is a complex quantity. Inserting this time-dependent vibrational overlap into eq 10 yields the full expression for the time-dependent the strong field ionization rate.

$$\text{rate } (t) = 2 \sum_{istate, jstate}^{Nstates} c_{istate}^{\text{el}*}(t) c_{jstate}^{\text{el}}(t)$$

$$\langle \Psi_{istate}^{\text{el}}(t) | \mathbf{V}^{\text{abs}} | \Psi_{jstate}^{\text{el}}(t) \rangle \times$$

$$\text{normal modes vibrational quanta}$$

$$\prod_{ivib} \sum_{v,v'} c_{v}^{ivib,istate} \times c_{v'}^{ivib,jstate} \times c_{v'}^{ivib,jstate}$$

$$\exp(i(E_{v}^{ivib,istate} - E_{v'}^{ivib,jstate}) t)$$

$$\langle \chi_{v}^{ivib,istate}(q_{ivib}) | \chi_{v'}^{ivib,jstate}(q_{ivib}) \rangle$$

$$(14)$$

The rate can also be written in terms of the reduced density matrix for the electronic states.

rate
$$(t) = \sum_{\substack{N \text{states} \\ \text{istate, jstate}}} \rho_{i\text{state, jstate}}^{\text{rdm}}(t) \langle \Psi_{i\text{state}}^{\text{el}}(t) | \mathbf{V}^{\text{abs}} | \Psi_{j\text{state}}^{\text{el}}(t) \rangle$$

$$\rho_{istate,jstate}^{\text{rdm}}(t) = c_{istate}^{\text{el*}}(t)c_{jstate}^{\text{el}}(t)\langle\Phi^{\text{vib},istate}(t)|\Phi^{\text{vib},jstate}(t)\rangle$$
(15)

Since $\langle \Phi^{\mathrm{vib},istate}(t)|\Phi^{\mathrm{vib},istate}(t)\rangle=1$, only the off-diagonal elements of the absorbing potential, $\langle \Psi^{\mathrm{el}}_{istate}(t)|\mathbf{V}^{\mathrm{abs}}|\Psi^{\mathrm{el}}_{jstate}(t)\rangle$, need to be multiplied by the vibrational overlap.

In the absence of a time-dependent field from a laser pulse and for frozen nuclei, the propagation of a superposition of states amounts to a time-dependent change in the phase factor of the superposition. For a superposition of the X and A states of HCCI⁺, expectation values (e.g., dipole moment) become time-dependent, reflecting the charge migration resulting from the coherent superposition.

$$\Psi_{XA}^{el}(t) = c_X \Psi_X^{el} + e^{-i\Delta E t} c_A e^{i\phi} \Psi_A^{el},$$

$$c_X^2 + c_A^2 = 1, c_X \text{ and } c_A \text{ real}$$
(16)

$$\begin{split} \langle \Psi^{\rm el}_{\rm XA}(t)|\mathbf{O}|\Psi^{\rm el}_{\rm XA}(t)\rangle &= c_{\rm X}^2 \langle \Psi^{\rm el}_{\rm X}|\mathbf{O}|\Psi^{\rm el}_{\rm X}\rangle + c_{\rm A}^2 \langle \Psi^{\rm el}_{\rm A}|\mathbf{O}|\Psi^{\rm el}_{\rm A}\rangle \\ &+ c_{\rm X}c_{\rm A}(\mathrm{e}^{-\mathrm{i}\Delta E t + \mathrm{i}\phi} \langle \Psi^{\rm el}_{\rm X}|\mathbf{O}|\Psi^{\rm el}_{\rm A}\rangle \\ &+ \mathrm{e}^{\mathrm{i}\Delta E t - \mathrm{i}\phi} \langle \Psi^{\rm el}_{\rm A}|\mathbf{O}|\Psi^{\rm el}_{\rm X}\rangle) \\ &= c_{\rm X}^2 \langle \Psi^{\rm el}_{\rm X}|\mathbf{O}|\Psi^{\rm el}_{\rm X}\rangle + c_{\rm A}^2 \langle \Psi^{\rm el}_{\rm A}|\mathbf{O}|\Psi^{\rm el}_{\rm A}\rangle \\ &+ \mathrm{cos}(\Delta E t - \phi)c_{\rm X}c_{\rm A}(\mathbf{O}_{\rm XA} + \mathbf{O}_{\rm AX}) \\ &+ \mathrm{sin}(\Delta E t - \phi)c_{\rm X}c_{\rm A}(\mathbf{O}_{\rm XA} - \mathbf{O}_{\rm AX}) \\ \\ \mathbf{O}_{\rm PQ} &= \langle \Psi^{\rm el}_{\rm P}|\mathbf{O}|\Psi^{\rm el}_{\rm Q}\rangle \end{split}$$

In the presence of a time-dependent field from a laser pulse, the electronic wavefunctions are time-dependent. In the TDCI approach, the propagation of the time-dependent coefficients is a solution of a set of linear differential equations. Any linear combination of solutions of a set of linear differential equations is also a solution. The ionization rate can be obtained from the expectation value of the absorbing potential (eq 10). For the superposition $\Psi_{XA}^{el}(0) = c_X \Psi_X^{el} + c_A e^{i\phi} \Psi_A^{el}$, the rate has contributions from the pure states and from cross terms.

$$\begin{aligned} \operatorname{rate}_{\operatorname{XA}}^{\operatorname{el}}(t) &= 2 \langle \Psi_{\operatorname{XA}}^{\operatorname{el}}(t) | \mathbf{V}^{\operatorname{abs}} | \Psi_{\operatorname{XA}}^{\operatorname{el}}(t) \rangle \\ &= 2 c_{\operatorname{X}}^2 \langle \Psi_{\operatorname{A}}^{\operatorname{el}}(t) | \mathbf{V}^{\operatorname{abs}} | \Psi_{\operatorname{X}}^{\operatorname{el}}(t) \rangle + 2 c_{\operatorname{A}}^2 \langle \Psi_{\operatorname{A}}^{\operatorname{el}}(t) | \\ & \mathbf{V}^{\operatorname{abs}} | \Psi_{\operatorname{A}}^{\operatorname{el}}(t) \rangle \\ &+ c_{\operatorname{X}} c_{\operatorname{A}} (\mathrm{e}^{i\phi} \langle \Psi_{\operatorname{X}}^{\operatorname{el}}(t) | \mathbf{V}^{\operatorname{abs}} | \Psi_{\operatorname{A}}^{\operatorname{el}}(t) \rangle + \mathrm{e}^{-i\phi} \langle \Psi_{\operatorname{A}}^{\operatorname{el}}(t) | \\ & \mathbf{V}^{\operatorname{abs}} | \Psi_{\operatorname{X}}^{\operatorname{el}}(t) \rangle) \\ &= 2 c_{\operatorname{X}}^2 \mathbf{V}_{\operatorname{XX}}(t) + 2 c_{\operatorname{A}}^2 \mathbf{V}_{\operatorname{AA}}(t) \\ &+ \cos(-\phi) c_{\operatorname{X}} c_{\operatorname{A}}(\mathbf{V}_{\operatorname{XA}}(t) + \mathbf{V}_{\operatorname{AX}}(t)) \\ &+ \sin(-\phi) c_{\operatorname{X}} c_{\operatorname{A}}(\mathbf{V}_{\operatorname{XA}}(t) - \mathbf{V}_{\operatorname{AX}}(t)) \end{aligned}$$

$$\mathbf{V}_{\operatorname{PQ}}(t) = \langle \Psi_{\operatorname{P}}^{\operatorname{el}}(t) | \mathbf{V}^{\operatorname{abs}} | \Psi_{\operatorname{Q}}^{\operatorname{el}}(t) \rangle \tag{18}$$

The real and imaginary components for these cross terms can be obtained from the rates for the X \pm A and X \pm *i*A superpositions.

$$\frac{1}{2}(\operatorname{rate}_{X+A}^{el}(t) - \operatorname{rate}_{X-A}^{el}(t))$$

$$= \langle \Psi_{X}^{el}(t)|\mathbf{V}^{abs}|\Psi_{A}^{el}(t)\rangle + \langle \Psi_{A}^{el}(t)|\mathbf{V}^{abs}|\Psi_{X}^{el}(t)\rangle$$

$$= (\mathbf{V}_{XA}(t) + \mathbf{V}_{AX}(t))$$

$$\frac{1}{2}(\operatorname{rate}_{X+iA}^{el}(t) - \operatorname{rate}_{X-iA}^{el}(t))$$

$$= i(\langle \Psi_{X}^{el}(t)|\mathbf{V}^{abs}|\Psi_{A}^{el}(t)\rangle$$

$$- \langle \Psi_{A}^{el}(t)|\mathbf{V}^{abs}|\Psi_{X}^{el}(t)\rangle)$$

$$= i(\mathbf{V}_{XA}(t) - \mathbf{V}_{AX}(t))$$
(19)

When nuclear motion is included, the electronic matrix elements of the absorbing potential need to be multiplied by the vibrational overlap, which is complex. Since the overlap is unity for the pure states, only the cross terms need to be multiplied by the vibrational overlap.

(17)

$$\begin{aligned} & \operatorname{rate}_{\mathrm{XA}}^{\mathrm{el}}(t) = 2 \langle \Psi_{\mathrm{XA}}^{\mathrm{el}}(t) | \mathbf{V}^{\mathrm{abs}} | \Psi_{\mathrm{XA}}^{\mathrm{el}}(t) \rangle \\ & \langle \Phi^{\mathrm{vib}, istate}(\mathbf{R}, t) | \Phi^{\mathrm{vib}, jstate}(\mathbf{R}, t) \rangle = 2 c_{\mathrm{X}}^{2} \mathbf{V}_{\mathrm{XX}}(t) \\ & + 2 c_{\mathrm{A}}^{2} \mathbf{V}_{\mathrm{AA}}(t) + c_{\mathrm{X}} c_{\mathrm{A}} (\mathrm{e}^{\mathrm{i}\phi} \mathbf{V}_{\mathrm{XA}}(t) S_{\mathrm{XA}}^{\mathrm{vib}}(t) \\ & + \mathrm{e}^{-\mathrm{i}\phi} \mathbf{V}_{\mathrm{AX}}(t) S_{\mathrm{AX}}^{\mathrm{vib}}(t)) = 2 c_{\mathrm{X}}^{2} \mathbf{V}_{\mathrm{XX}}(t) + 2 c_{\mathrm{A}}^{2} \mathbf{V}_{\mathrm{AA}}(t) \\ & + \cos(-\phi) c_{\mathrm{X}} c_{\mathrm{A}} \\ & [(\mathbf{V}_{\mathrm{XA}}(t) + \mathbf{V}_{\mathrm{AX}}(t)) (S_{\mathrm{XA}}^{\mathrm{vib}}(t) \\ & + S_{\mathrm{AX}}^{\mathrm{vib}}(t)) + (\mathbf{V}_{\mathrm{XA}}(t) - \mathbf{V}_{\mathrm{AX}}(t)) (S_{\mathrm{XA}}^{\mathrm{vib}}(t) - S_{\mathrm{AX}}^{\mathrm{vib}}(t))] \\ & + \sin(-\phi) c_{\mathrm{X}} c_{\mathrm{A}} \\ & [(\mathbf{V}_{\mathrm{XA}}(t) + \mathbf{V}_{\mathrm{AX}}(t)) (S_{\mathrm{XA}}^{\mathrm{vib}}(t) - S_{\mathrm{AX}}^{\mathrm{vib}}(t)) \\ & + (\mathbf{V}_{\mathrm{XA}}(t) - \mathbf{V}_{\mathrm{AX}}(t)) (S_{\mathrm{XA}}^{\mathrm{vib}}(t) + S_{\mathrm{AX}}^{\mathrm{vib}}(t))] S_{\mathrm{PQ}}^{\mathrm{vib}}(t) \\ & = \langle \Phi_{\mathrm{P}}^{\mathrm{vib}}(\mathbf{R}, t) | \Phi_{\mathrm{Q}}^{\mathrm{vib}}(\mathbf{R}, t) \rangle \end{aligned} \tag{20}$$

A locally modified version of the Gaussian software package⁶² was used to calculate the CAP integrals needed for the TDCI simulation. The aug-cc-pVTZ basis set was used for H and C; 63-65 the aug-cc-pVTZ-PP basis set with pseudopotential was used for iodine. 66 Additional diffuse functions were placed on each atom to describe the electron dynamics during the ionization process and to ensure adequate interaction with the CAP. This set of basis functions consisted of four s functions (exponents of 0.0256, 0.0128, 0.0064, and 0.0032), four p functions (exponents of 0.0256, 0.0128, 0.0064, and 0.0032), five d functions (exponents of 0.0512, 0.0256, 0.0128, 0.0064, and 0.0032) and two f function (exponent of 0.0256 and 0.0128). 37,54 The electronic wavefunction for HCCI included all excitations from the highest σ orbital and two highest pairs of π orbitals to all virtual orbitals with orbital energies less than 3 hartree (1 hartree = 27.2114 eV), for a total of 2621 configurations for HCCI neutral and 18530 configurations for HCCI cations. The spherical absorbing potential on each atom was chosen to start at approximately 3.5 times the van der Waals radius. The parameters of the potentials were $V_{\rm max}$ = 10 hartree, R_A = 14.882, 12.735, and 9.544 bohr for I, C, and H, respectively, and $R_B = 43.166$, 41.020, and 37.828 bohr for I, C, and H respectively (1 bohr = 0.529177 Å). The TDCI simulations were carried out with an external Fortran95 code. Mathematica⁶⁷ was used to calculate the vibrational components of the reduced density matrix and ionization rate and to analyze the simulations and plot the results.

RESULTS AND DISCUSSION

The TDCI calculation of the electronic component of the strong field ionization of HCCI has been described previously 60 and is summarized briefly here. The π and π^* orbitals of HCCI are the in-phase and out-of-phase combinations of the C \equiv C π orbitals and the iodine π -type lone pairs (Figure 2a). Removing an electron from the π^* orbital produces the X state of the cation, while removing an electron from the π orbital produces the A state of the cation. Since the σ orbital is 0.2 hartree lower in energy than the π^* orbital, it does not contribute significantly to ionization at the field strength used in this study. The angular dependence of the ionization rate for neutral HCCI is shown in Figure 2b. When averaged over all directions, the calculated ratio of the ionization yields for the X and A states is 3.9, which is in good agreement with the experimental ratio of 4.3 reconstructed from the higher harmonic spectra.

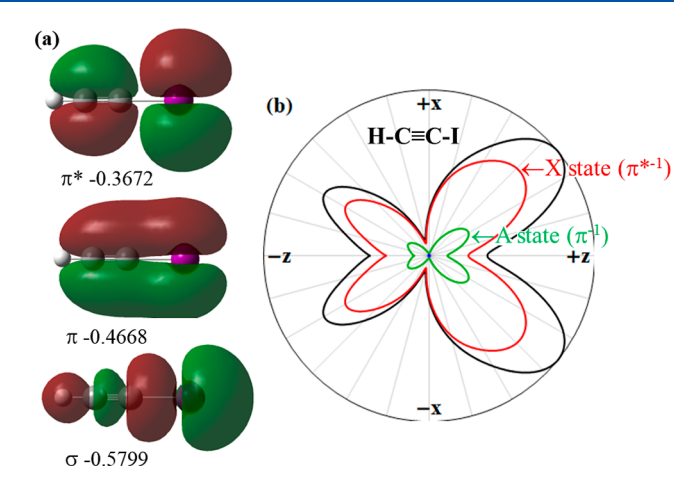


Figure 2. (a) Highest occupied orbitals of HCCI and their orbital energies in atomic units (1 hartree = 27.2114 eV). (b) Angular dependence of the instantaneous ionization rate for neutral HCCI in the static field of $1.70\,\mathrm{V/Å} = 0.033\,\mathrm{au}$ (total ionization rate in black and yield of X and A states of the cation in red and green, respectively).

Strong field ionization of HCCI can produce a coherent superposition of the X and A states of the cation that results in charge migration between the $C \equiv C \pi$ orbital and the iodine π -type lone pair. Snapshots of the hole migration are shown in Figure 3 for frozen nuclei. The period for the field-free charge migration, 1.87 fs, depends on the energy difference between the X and A states. The energy difference calculated by CISD-IP (2.21 eV) is in very good agreement with the value from the experiment (2.23 eV).

Strong field ionization can be used to probe the charge migration. The ionization is highest from the iodine end (i.e., highest when the electron hole is on $C \equiv C$ rather than on I). Figure 4 shows the ionization rate for HCCI with frozen nuclei for a 7-cycle linear pulse with CEP = $\pi/2$ and polarization perpendicular to the molecular axis. The ionization rate depends on the initial phase for the superposition, $X + e^{i\phi} A$ at t = 0. The rate also depends on the time for propagation of the superposition from t = 0 to the two most intense peaks in the pulse at t = 8.65 and 9.98 fs. The maximum ionization rate for the second peak in the pulse is offset from the maximum in the first peak as a result of charge migration during the time between the two peaks (1.33 fs). A pulse perpendicular to the molecular axis does not significantly alter the period for charge migration because the permanent dipoles for the X and A states and the transition dipole between the X and A states are perpendicular to the electric field of the pulse. The dynamics of the charge migration are more complicated for other orientations of the pulse because the charge migration can be driven by the component of the electric field of the pulse along the molecular axis in addition to the intrinsic oscillation due to the coherent superposition.

When nuclear motion is included, the results are modified by the overlap between the vibrational wavepackets on the X and A surfaces. The shape and overlap of the wavepackets depend on the differences in the geometry and vibrational frequencies of the neutral ground state and of the two cations, as summarized in Table 1. The geometries for the ground state and cations were adopted from high-level calculations in a previous study. Experimental vibrational frequencies were obtained from the literature. ^{69,70} No C–H stretch frequency was available for the A state; the value from the X state was used since the C–H bond

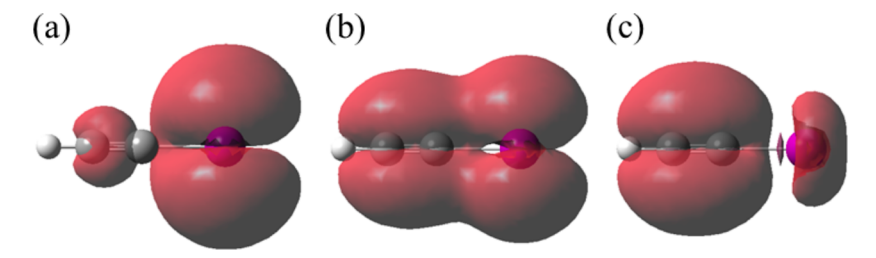


Figure 3. Field-free coherent superposition of the X and A states of the HCCI cation. Hole density for (a) X + A, (b) X + iA, and (c) X - A.

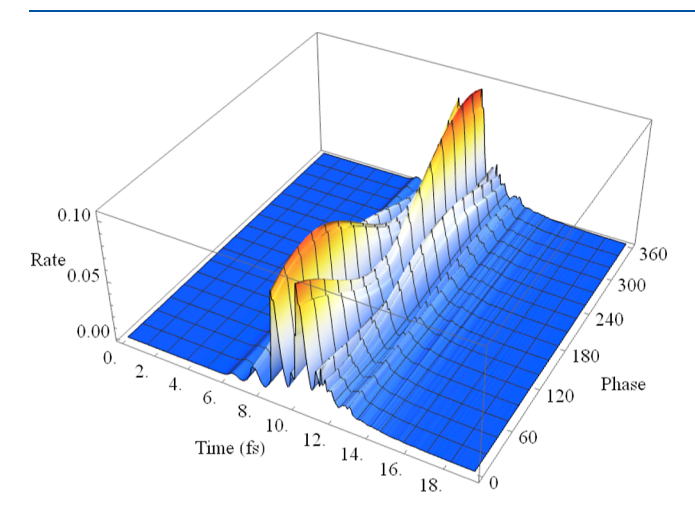


Figure 4. Ionization rate HCCI⁺ with frozen nuclei as a function of time and the initial phase of the superposition $(X + e^{i\phi}A)$ for a 7-cycle linearly polarized 800 nm pulse with CEP = $\pi/2$ and a maximum intensity of $1.97 \times 10^{14} \text{ W cm}^{-2} (E_{\text{max}} = 3.86 \text{ V/Å} = 0.075 \text{ au})$ for polarization perpendicular to the molecular axis.

Table 1. Geometry and Vibrational Frequencies for HCCI Neutral and $Cations^a$

	HCCI ground state	HCCI ⁺ X state	HCCI ⁺ A state
R(C-I)	2.0244 Å	1.9515 Å	2.1483 Å
$R(C \equiv C)$	1.2169 Å	1.2392 Å	1.2457 Å
R(C-H)	1.0746 Å	1.0828 Å	1.0838 Å
$\nu({\rm CI~str})$	490 cm^{-1}	578 cm^{-1}	407 cm^{-1}
$\nu(\text{CC str})$	2060 cm^{-1}	1805 cm^{-1}	1822 cm^{-1}
$\nu(\mathrm{CH}\;\mathrm{str})$	3360 cm^{-1}	3258 cm^{-1}	3258 cm^{-1}

^aGeometries from ref 4 calculated at CASSCF/cc-pVQZ; experimental frequencies from refs 69 and 70.

lengths differ by only 0.001 Å. Because the cations are linear, only the symmetric vibrational modes will be excited on ionization. It has been shown that the remaining, asymmetric vibrational modes do not significantly affect the dynamics of the coherent superposition.⁷¹ Yang and co-workers have demonstrated that employing the 3 symmetric vibrational modes for HCCI⁺ gives

essentially the same results as using all 7 vibrational modes. ^{11–13} Normal modes for the neutral ground state of HCCI were calculated with the CCSD/aug-cc-pVTZ level of theory (see Table 2). The minima for the potential energy surface for the cations are displaced from the minimum for the neutral ground state. The displacements in terms of the normal modes were obtained by projecting the geometry differences onto the normal modes.

Vertical ionization produces vibrational wavepackets on the potential energy surfaces of the ionized states. In the Franck-Condon approximation, the wavepackets are obtained from the overlap between the vibrational wavefunction on the neutral ground state surface with the vibrational wavefunctions on the cation surfaces. In the present study of HCCI, the vibrational wavefunctions are approximated by harmonic oscillator functions with the frequencies and displacements listed in Tables 1 and 2. As in the study by Yang and co-workers, 11 the normal modes for the ionized states are chosen to be the same as for the neutral and coupling between the vibrational modes in the cations is ignored. The overlaps between the zero-point vibrational wavefunction of the ground state and the vibrational wavefunctions for the cations provide the initial coefficients for the wavepackets on the X and A states of the cation, in accord with the Franck-Condon principle. Since the cation surfaces are approximated by harmonic potentials, the dynamics of the wavepacket can be calculated analytically (see eqs 11 and 12). This approach has been used previously by various authors in a number of studies 11-13,51,52 and was found to be satisfactory for modeling electronic decoherence resulting from nuclear dynamics of HCCI⁺ and for similar molecules. It has been shown that transitions between the X and A states of the cation can be ignored for the time lengths in the present simulations.⁴ Therefore, vibrational wavepackets on the potential energy surfaces for the X and A states move independently.

The largest movements of the vibrational wavepackets are seen for the C–I stretching mode because the differences in the frequencies and displacements from the ground state are largest. As shown in Figure 5, the C–I stretch wavepacket on the X state initially moves toward a shorter C–I bond length and the wavepacket on the A state moves toward a longer bond length. The C–I overlap decreases by half in about 6 fs and is near zero

Table 2. Normal Modes and Displacement for HCCI Neutral and Cations^a

	HCCI normal mode components			HCCI ⁺ X state displacement	HCCI ⁺ A state displacement
	R(C-I)	R(C≡C)	R(C-H)		
C–I str mode	0.6274	0.0731	0.0181	−0.09002 Å	0.20974 Å
C≡C str mode	-0.5333	0.9368	0.3356	0.03076 Å	0.01446 Å
C-H str mode	0.0304	-0.1430	1.1059	−0.00045 Å	0.00050 Å

[&]quot;Normal modes calculated for the ground state with CCSD/aug-cc-pVTZ; displacements obtained by projecting geometry changes onto the normal modes; reduced masses for the C−I str, C≡C str and C−H str modes are 9.3062, 5.9129, and 1.1576 amu, respectively.

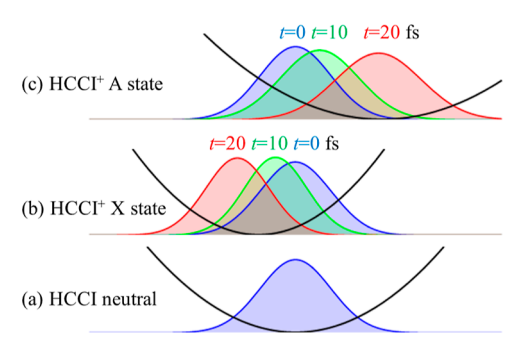


Figure 5. Vibrational wavepackets for C-I stretch for neutral HCCI and X and A states at (a) 0 fs (blue), (b) 10 fs (green), and (c) 20 fs (red). Potential energy curves are shown in black.

by 20 fs. Because the initial wavepackets are Gaussian-shaped, the C–I overlap decreases as a Gaussian function as the wavepackets move away from each other.

The total overlap is a product of the overlaps for the individual modes. The variation of the overlaps with time is shown in Figure 6. The displacements and difference in the frequencies are much

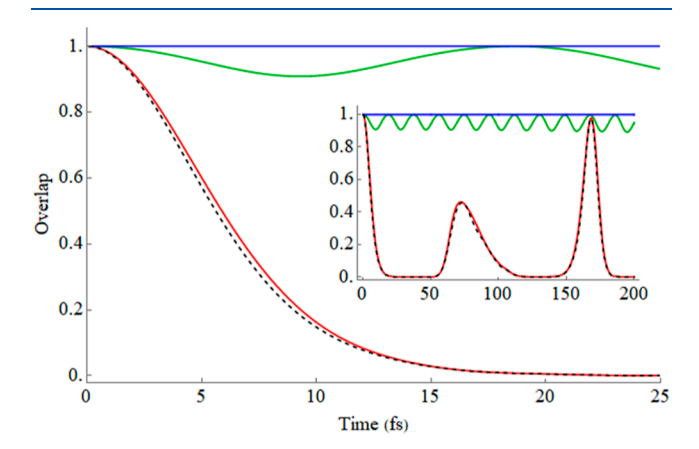


Figure 6. Absolute value of the overlap of vibrational wavepackets on the X and A states of HCCI⁺ for the C−I stretch (red), C≡C stretch (green), and C−H stretch (blue). The absolute value of the product of the overlaps for the three modes is shown in dashed black. The inset shows revivals of the overlap near 70 and 170 fs.

smaller for the C \equiv C stretch; the overlap between the C \equiv C wavepackets on the X and A surfaces changes by less than 10%. The overlap for the C-H stretch is nearly constant because the displacements are very small and the frequencies are identical. The absolute value of the product of the C-I stretch, C \equiv C stretch, and C-H stretch overlaps is dominated by the C-I stretch. In the absence of decay mechanisms, the wavepackets on the X and A states return to the Franck-Condon region and overlap again, as shown in the inset in Figure 6. These results are in excellent agreement with those of Yang and co-workers. ¹¹

The ionization rates for HCCI⁺ in a static field oriented perpendicular to the molecular axis are shown in Figure 7 for the X + A coherent superposition. The oscillation frequency for the ionization rate is determined by the energy difference between the two states. The total ionization rate with moving nuclei is given by the electronic (fixed nuclei) ionization rates times the vibrational overlap factor (eq 14). The diagonal terms of the electronic ionization rates are given by simulations with pure X and A states, and the vibrational overlap is 1. The off-diagonal terms for the electronic contribution can be obtained from

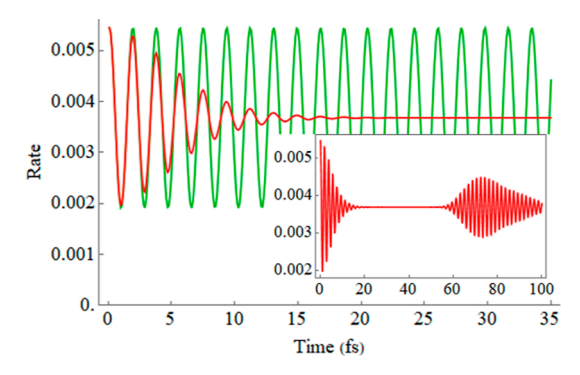


Figure 7. Oscillation of the ionization rate for the coherent X+A superposition for HCCI $^+$ in a static field of 2.83 V/Å = 0.055 au (1.97 × 10^{14} W cm $^{-2}$) perpendicular to the molecular axis. When the nuclei are frozen, coherent electronic oscillations continue undamped (green). When nuclear motion is included, coherent oscillations decay in about 10-15 fs. The inset shows the oscillation in the ionization rate are visible again in the first revival, 60-110 fs.

simulations with $X \pm A$ and $X \pm iA$ coherent superpositions, as described in eq 19 of the Methods Section. The corresponding components were calculated previously for a static field of 2.83 V/Å = 0.055 au $(1.97 \times 10^{14} \,\mathrm{W}\,\mathrm{cm}^{-2})$ oriented perpendicular to the molecular axis. 60 When the nuclei are fixed, the ionization rate oscillates continuously without decay (green line in Figure 7). When the nuclei are allowed to move, the absolute value of the overlap of the vibrational wavepackets for the X and A states quickly goes to zero (Figure 6). The oscillations in the ionization rate decay in about 10–15 fs (red line in Figure 7). About 7 oscillations are visible. In the absence of additional decay mechanisms, the oscillations in the ionization rate persist in the first revival when the vibrational overlap becomes non-zero again (inset in Figure 7). The previous computational studies of charge migration in HCCI+ by Yang and co-workers 11,12 found very similar results for the decoherence and recoherence of the electron flux along the molecular axis.

A coherent superposition of cations states can be produced by strong field ionization using a short, intense pulse. From higher harmonic spectra of aligned HCCI, Kraus et al. were able to reconstruct the coefficients and relative phase of the coherent superposition of the X and A states of HCCI+. They obtained $\Psi_{\rm XA}^{\rm el}=c_{\rm X}{\rm X}+c_{\rm A}{\rm e}^{i\phi_0}{\rm A}=0.90~{\rm X}+0.43{\rm e}^{-0.34i}{\rm A}$ for the initial superposition produced by strong field ionization. This superposition reconstructed from experiment has been used in our simulations of charge migration probed by a second short, intense pulse that ionizes the cation to the dication. During the time delay between the pump and probe pulses, the phase of the superposition, $\Psi_{XA}^{el} = c_X X + c_A e^{i\phi} A = c_X X + c_A e^{-\Delta E t + i\phi_0} A$, evolves with a field-free period of $\tau = 1.87$ fs. Figure 8 shows the ionization rate of the $\Psi^{
m el}_{
m XA}$ superposition for a 2-cycle 800 nm linearly polarized pulse perpendicular to the molecular axis as a function of the time delay. The maximum in the ionization rate occurs when the electron density on iodine is highest at the peak in the field. When nuclear motion is included, the vibrational wavepackets of the X and A states move away from each other, and the vibrational overlap decreases, as seen in Figure 5. With no initial delay, the peak in the probe pulse is at 2.66 fs, and the absolute value of the vibrational overlap is 0.85. The variation in the ionization rate at short delay times is only slightly diminished. As the pulse is delayed for up to 5 fs, the overlap of the vibrational wavepackets decreases to 0.30 and the variation in the ionization

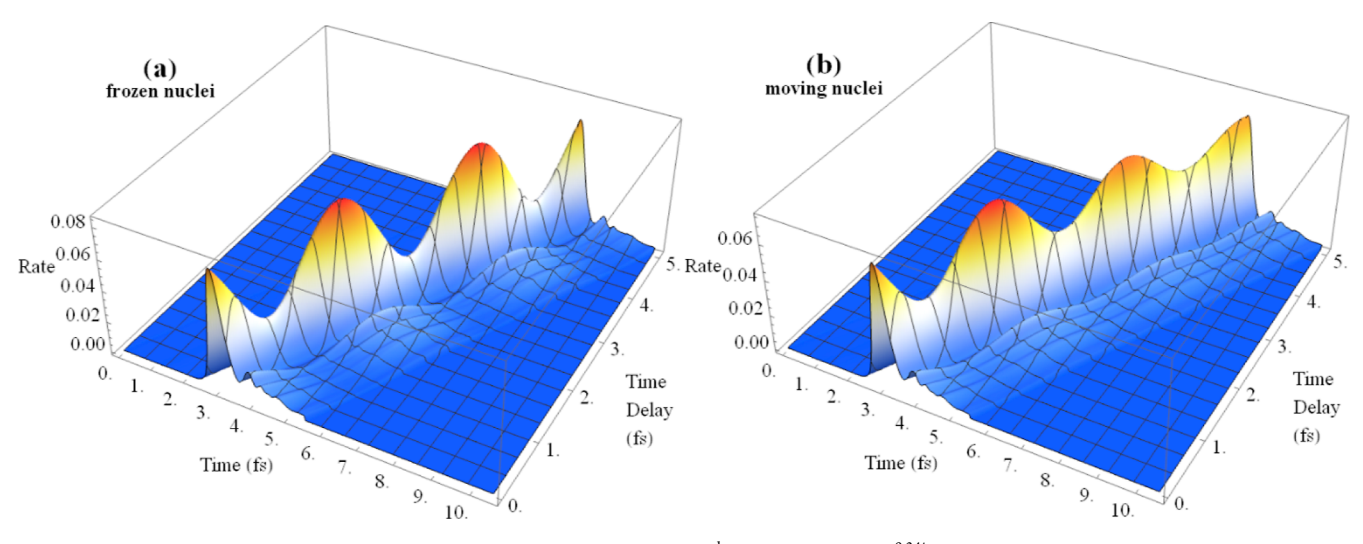


Figure 8. Ionization rate as a function of time and probe pulse delay for the $\Psi^{el}_{XA} = 0.90 \text{ X} + 0.43 \text{e}^{-0.34i} \text{A}$ superposition with a 2-cycle linearly polarized 800 nm pulse with CEP = 0 and a maximum intensity of $1.97 \times 10^{14} \text{ W cm}^{-2}$ for polarization perpendicular to the molecular axis: (a) frozen nuclei and (b) nuclear wavepackets moving on quadratic surfaces for the X and A states.

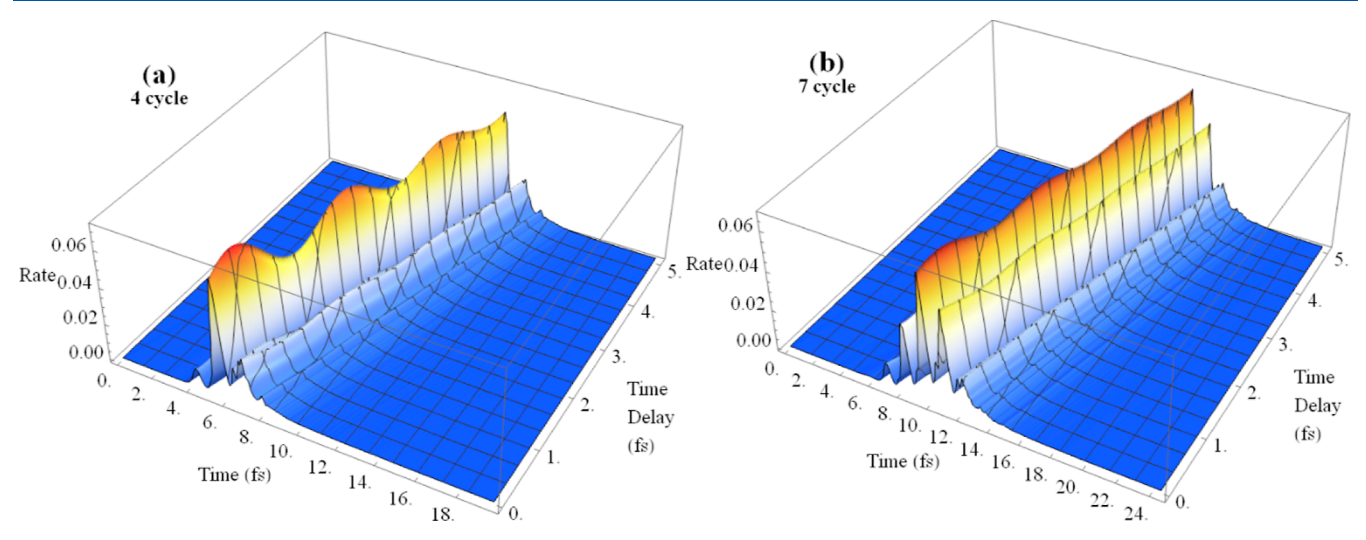


Figure 9. Ionization rate as a function of time and probe pulse delay for the $\Psi^{el}_{XA} = 0.90 \text{ X} + 0.43 \text{e}^{-0.34i} \text{A}$ superposition with (a) 4-cycle and (b) 7-cycle linearly polarized 800 nm pulses with CEP = 0 and a maximum intensity of $1.97 \times 10^{14} \text{ W cm}^{-2}$ for polarization perpendicular to the molecular axis and nuclear wavepackets moving on quadratic surfaces for the X and A states.

rate with delay time is noticeably smaller. Figure 9 shows the effect of delay on 4- and 7-cycle pulses. The peak ionization rate for a 4-cycle pulse occurs at 5.33 fs; as the delay times increases to 5 fs, the variation in the ionization rate becomes smaller as the vibrational overlap drops to 0.13. The peak ionization rate for a 7-cycle pulse is at 9.3 fs, and the ionization rate is nearly constant beyond a 3 fs delay.

Integration of the ionization rate over the duration of the pulse gives the ionization yield and is shown for various delay times in Figure 10. Most of the ionization from the cation to the dication occurs in a small time interval around the peak in the probe pulse, as shown in Figures 8 and 9. With no delay in the start of the probe pulse, the peaks in the 2-, 4-, and 7-cycle pulses occur at 2.66, 5.33, and 9.3 fs, respectively, and the absolute values of the vibrational overlap factors are 0.85, 0.53, and 0.18, respectively (black dashed line in Figure 10). As the delay time is increased, the peaks in the probe pulses are shifted to later times and the vibrational overlap factor decreases further. This dampens the oscillation in the ionization yield for longer times. Nevertheless,

oscillation in the ionization yield due to charge migration can be seen for 2- and 4-cycle pulses at short delay times.

At delay times of 60–110 and 150–180 fs, there are revivals in the vibrational overlap factor as the wavepackets on the X and A surfaces return to the Franck–Condon region (see Figure 6). The maximum in the absolute value of the overlap reaches 0.46 in the first revival. In the absence of decay mechanisms, the electronic part of the wavefunction is still a superposition of the X and A states. Consequently, there is also a revival in the variation in the strong field ionization yield that results from charge migration, as shown in Figure 11. For a 2-cycle pulse, the variation in the ionization yield is comparable to that seen for very short delay times. For a 4-cycle pulse, the variation in the ionization yield is approximately 9% of the total yield and should be readily observable. For a 7-cycle pulse, the variation is only 2% and may be more difficult to detect.

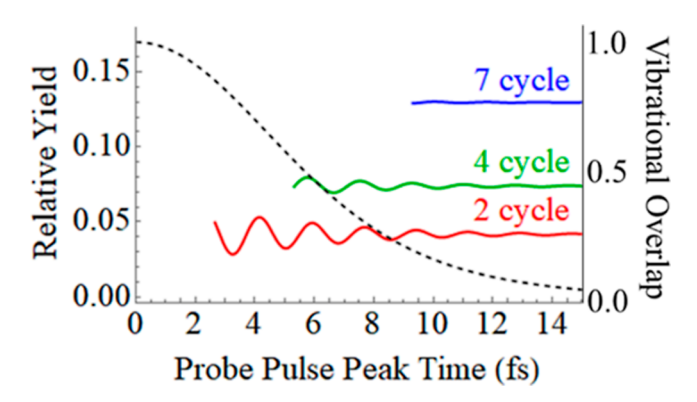


Figure 10. Ionization yield for the $\Psi_{\rm XA}^{\rm el}=0.90~{\rm X}+0.43{\rm e}^{-0.34{\rm i}}{\rm A}$ superposition versus the time of the peak in the probe pulse for various delay times for 2-, 4-, and 7-cycle linearly polarized 800 nm pulses with CEP = 0 and a maximum intensity of $1.97\times10^{14}\,{\rm W\,cm}^{-2}$ perpendicular to the molecular axis and nuclear wavepackets moving on quadratic surfaces for the X and A states. The dashed black curve is the absolute value of the vibrational overlap.

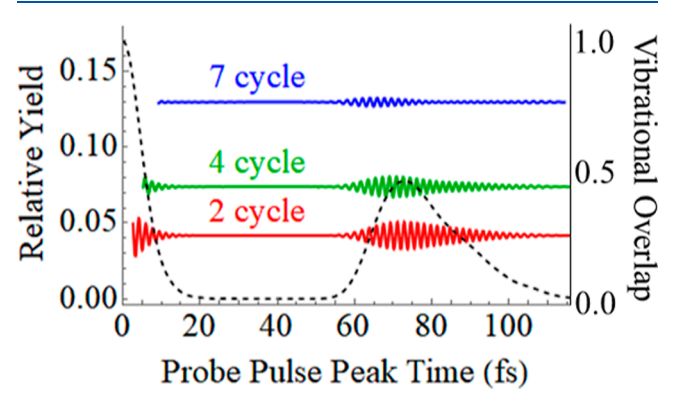


Figure 11. Revival of ionization yield for the $\Psi_{XA}^{el} = 0.90 \text{ X} + 0.43 \text{ e}^{-0.34\text{i}} \text{A}$ superposition versus the time of the peak in the probe pulse for various delay times for 2-, 4-, and 7-cycle linearly polarized 800 nm pulses with CEP = 0 and a maximum intensity of $1.97 \times 10^{14} \text{ W cm}^{-2}$ perpendicular to the molecular axis and nuclear wavepackets moving on quadratic surfaces for the X and A states. The dashed black curve is the absolute value of the vibrational overlap.

SUMMARY

Strong field ionization can be used to produce a coherent superposition of cationic states and to probe the dynamics of this superposition by ionizing the cations to dications. The dynamics of HCCI⁺ have been studied extensively by both experimental and theoretical methods.^{4,9–13} The coherent superposition of the X and A states of HCCI⁺ leads to charge migration between the C \equiv C π orbital and the iodine π -type lone pair. The electronic dynamics of charge migration is coupled with nuclear dynamics as the vibrational wavepackets evolve separately on the potential energy surfaces of the X and A states. TDCI with a CAP has been used to simulate the electronic dynamics and strong field ionization of coherent superpositions of the X and A states of HCCI⁺. A CISD-IP wavefunction consisting of singly ionized and singly excited, singly ionized configurations was used to treat the α and β spin-orbitals of the cation equivalently and to treat the π_x and π_y orbitals equivalently. The electronic component of ionization rate is given by the rate of decrease in the norm squared of the electronic wavefunction as the electron density is absorbed by the CAP. The charge migration is observable as an oscillation in the electronic component of the ionization rate as

the charge moves between the C \equiv C π orbital and the iodine π type lone pair. Nuclear motion was modeled by vibrational packets moving on quadratic approximations to the potential energy surfaces for the X and A states of the cation. Experimental vibrational frequencies and calculated geometries were used to construct the cation potential energy surfaces. The normal modes of vibration for the cations were assumed to be the same as for the ground state; non-adiabatic coupling between the surfaces and intermode coupling of the vibrations were ignored. The simulations included the C−I stretch, C≡C stretch, and C-H stretch modes since only the symmetric modes contribute significantly to the wavepacket dynamics for the superposition of the cations generated by strong field ionization. The total rate is given by the electronic component (matrix element of the absorbing potential) multiplied by the vibrational component (overlap of the vibrational wavepackets on the X and A surfaces). The vibrational wavepackets on the two surfaces initially move away from each other and their overlap decays to zero in about 15-20 fs. Consequently, the oscillations in the strong field ionization decay at the same rate. TDCI simulations with the coherent superposition reconstructed from experiment show that the oscillations in the ionization yield and charge migration can be monitored by strong field ionization with intense 2- and 4cycle linearly polarized 800 nm probe pulses for delay times of up to 10 and 5 fs, respectively. A revival of the vibrational overlap is seen between 60 and 110 fs when the vibrational wavepackets on the X and A surfaces both return to the Franck-Condon region. TDCI simulations show that the charge migration during this revival can be seen by strong field ionization with intense 2-, 4-, and 7-cycle probe pulses.

While the 2-cycle pulses used in the present study are still challenging experimentally, the generation of 4-cycle pulses is already feasible. The simulations use linear pulses with polarizations perpendicular to the molecular axis. In this orientation, the probe pulses do not cause transitions between the X and A states and do not alter the intrinsic frequency of charge migration along the molecular axis. For other orientations of linearly polarized pulses and for circularly polarized pulses, the field of the probe pulse can drive the electron density along the molecular axis, leading to more complicated charge migration dynamics that is a combination of the intrinsic frequency and the frequency of the laser field.

AUTHOR INFORMATION

Corresponding Author

H. Bernhard Schlegel — Department of Chemistry, Wayne State University, Detroit, Michigan 48202, United States;
ocid.org/0000-0001-7114-2821; Email: hbs@chem.wayne.edu

Complete contact information is available at: https://pubs.acs.org/10.1021/acs.jpca.3c02667

Notes

The author declares no competing financial interest.

ACKNOWLEDGMENTS

The author wishes to thank Prof. Wen Li for stimulating discussions on strong field ionization and coherence. This work was supported by a grant from the National Science Foundation (CHE1856437) and U.S. Department of Energy, Office of Science, Basic Energy Sciences (award no. DE-SC0020994).

The author thanks the Wayne State University computing grid for computer time.

REFERENCES

- (1) Smirnova, O.; Patchkovskii, S.; Mairesse, Y.; Dudovich, N.; Ivanov, M. Y. Strong-field control and spectroscopy of attosecond electron-hole dynamics in molecules. *Proc. Natl. Acad. Sci. U.S.A.* **2009**, *106*, 16556–16561
- (2) Goulielmakis, E.; Loh, Z. H.; Wirth, A.; Santra, R.; Rohringer, N.; Yakovlev, V. S.; Zherebtsov, S.; Pfeifer, T.; Azzeer, A. M.; Kling, M. F.; et al. Real-time observation of valence electron motion. *Nature* **2010**, 466, 739–743.
- (3) Calegari, F.; Ayuso, D.; Trabattoni, A.; Belshaw, L.; De Camillis, S.; Anumula, S.; Frassetto, F.; Poletto, L.; Palacios, A.; Decleva, P.; et al. Ultrafast electron dynamics in phenylalanine initiated by attosecond pulses. *Science* **2014**, *346*, *336*–*339*.
- (4) Kraus, P. M.; Mignolet, B.; Baykusheva, D.; Rupenyan, A.; Horný, L.; Penka, E. F.; Grassi, G.; Tolstikhin, O. I.; Schneider, J.; Jensen, F.; et al. Measurement and laser control of attosecond charge migration in ionized iodoacetylene. *Science* **2015**, *350*, 790–795.
- (5) Matselyukh, D. T.; Despre, V.; Golubev, N. V.; Kuleff, A. I.; Worner, H. J. Decoherence and revival in attosecond charge migration driven by non-adiabatic dynamics. *Nat. Phys.* **2022**, *18*, 1206–1213.
- (6) Kienberger, R.; Goulielmakis, E.; Uiberacker, M.; Baltuska, A.; Yakovlev, V.; Bammer, F.; Scrinzi, A.; Westerwalbesloh, T.; Kleineberg, U.; Heinzmann, U.; Drescher, M.; et al. Atomic transient recorder. *Nature* **2004**, *427*, 817–821.
- (7) Eckle, P.; Smolarski, M.; Schlup, P.; Biegert, J.; Staudte, A.; Schoffler, M.; Muller, H. G.; Dorner, R.; Keller, U. Attosecond angular streaking. *Nat. Phys.* **2008**, *4*, 565–570.
- (8) Winney, A. H.; Lee, S. K.; Lin, Y. F.; Liao, Q.; Adhikari, P.; Basnayake, G.; Schlegel, H. B.; Li, W. Attosecond electron correlation dynamics in double ionization of benzene probed with two-electron angular streaking. *Phys. Rev. Lett.* **2017**, *119*, 123201.
- (9) Ding, H.; Jia, D.; Manz, J.; Yang, Y. G. Reconstruction of the electronic flux during adiabatic attosecond charge migration in HCCI⁺. *Mol. Phys.* **2017**, *115*, 1813–1825.
- (10) Jenkins, A. J.; Spinlove, K. E.; Vacher, M.; Worth, G. A.; Robb, M. A. The Ehrenfest method with fully quantum nuclear motion (Qu-Eh): Application to charge migration in radical cations. *J. Chem. Phys.* **2018**, 149, 094108.
- (11) Jia, D.; Manz, J.; Yang, Y. De- and recoherence of charge migration in ionized iodoacetylene. *J. Phys. Chem. Lett.* **2019**, *10*, 4273–4277.
- (12) Jia, D.; Manz, J.; Yang, Y. Timing the recoherences of attosecond electronic charge migration by quantum control of femtosecond nuclear dynamics: A case study for HCCI*. *J. Chem. Phys.* **2019**, *151*, 244306.
- (13) Jia, D.; Yang, Y. Systematic investigation of the reliability of the frozen nuclei approximation for short-pulse excitation: The example of HCCI⁺. *Front. Chem.* **2022**, *10*, 857348.
- (14) Bandrauk, A. D.; Chelkowski, S.; Corkum, P. B.; Manz, J.; Yudin, G. L. Attosecond photoionization of a coherent superposition of bound and dissociative molecular states: effect of nuclear motion. *J. Phys. B: At. Mol. Opt. Phys.* **2009**, *42*, 134001.
- (15) Yuan, K. J.; Bandrauk, A. D. Time-Resolved Photoelectron Imaging of Molecular Coherent Excitation and Charge Migration by Ultrashort Laser Pulses. *J. Phys. Chem. A* **2018**, *122*, 2241–2249.
- (16) Posthumus, J. H. The dynamics of small molecules in intense laser fields. *Rep. Prog. Phys.* **2004**, *67*, 623–665.
- (17) Ishikawa, K. L.; Sato, T. A review on ab initio approaches for multielectron dynamics. *IEEE J. Sel. Top. Quantum Electron.* **2015**, 21, 1–16.
- (18) Nisoli, M.; Decleva, P.; Calegari, F.; Palacios, A.; Martin, F. Attosecond electron dynamics in molecules. *Chem. Rev.* **2017**, *117*, 10760–10825.
- (19) Goings, J. J.; Lestrange, P. J.; Li, X. S. Real-time time-dependent electronic structure theory. *Wiley Interdiscip. Rev.: Comput. Mol. Sci.* **2018**, 8, No. e1341.

- (20) Li, X. S.; Govind, N.; Isborn, C.; DePrince, A. E.; Lopata, K. Real-Time Time-Dependent Electronic Structure Theory. *Chem. Rev.* **2020**, *120*, 9951–9993.
- (21) Palacios, A.; Martin, F. The quantum chemistry of attosecond molecular science. *Wiley Interdiscip. Rev.: Comput. Mol. Sci.* **2020**, *10*, No. e1430.
- (22) Tong, X. M.; Zhao, Z. X.; Lin, C. D. Theory of molecular tunneling ionization. *Phys. Rev. A* **2002**, *66*, 033402.
- (23) Tolstikhin, O. I.; Morishita, T.; Madsen, L. B. Theory of tunneling ionization of molecules: Weak-field asymptotics including dipole effects. *Phys. Rev. A* **2011**, *84*, 053423.
- (24) Chu, X. Time-dependent density-functional-theory calculation of strong-field ionization rates of H₂. Phys. Rev. A **2010**, 82, 023407.
- (25) Chu, X.; Chu, S. I. Time-dependent density-functional theory for molecular processes in strong fields: Study of multiphoton processes and dynamical response of individual valence electrons of N₂ in intense laser fields. *Phys. Rev. A* **2001**, *64*, 063404.
- (26) Hellgren, M.; Rasanen, E.; Gross, E. K. U. Optimal control of strong-field ionization with time-dependent density-functional theory. *Phys. Rev. A* **2013**, *88*, 013414.
- (27) Lopata, K.; Govind, N. Near and above ionization electronic excitations with non-hermitian real-time time-dependent density functional theory. *J. Chem. Theory Comput.* **2013**, *9*, 4939–4946.
- (28) Provorse, M. R.; Isborn, C. M. Electron dynamics with real-time time-dependent density functional theory. *Int. J. Quantum Chem.* **2016**, 116, 739–749.
- (29) Bruner, A.; Hernandez, S.; Mauger, F.; Abanador, P. M.; LaMaster, D. J.; Gaarde, M. B.; Schafer, K. J.; Lopata, K. Attosecond charge migration with TDDFT: Accurate dynamics from a well-defined initial state. *J. Phys. Chem. Lett.* **2017**, *8*, 3991–3996.
- (30) Sandor, P.; Sissay, A.; Mauger, F.; Abanador, P. M.; Gorman, T. T.; Scarborough, T. D.; Gaarde, M. B.; Lopata, K.; Schafer, K. J.; Jones, R. R. Angle dependence of strong-field single and double ionization of carbonyl sulfide. *Phys. Rev. A* **2018**, *98*, 043425.
- (31) Krause, P.; Klamroth, T.; Saalfrank, P. Time-dependent configuration-interaction calculations of laser-pulse-driven many-electron dynamics: Controlled dipole switching in lithium cyanide. *J. Chem. Phys.* **2005**, *123*, 074105.
- (32) Rohringer, N.; Gordon, A.; Santra, R. Configuration-interaction-based time-dependent orbital approach for ab initio treatment of electronic dynamics in a strong optical laser field. *Phys. Rev. A* **2006**, *74*, 043420.
- (33) Krause, P.; Klamroth, T.; Saalfrank, P. Molecular response properties from explicitly time-dependent configuration interaction methods. *J. Chem. Phys.* **2007**, *127*, 034107.
- (34) Klinkusch, S.; Saalfrank, P.; Klamroth, T. Laser-induced electron dynamics including photoionization: A heuristic model within time-dependent configuration interaction theory. *J. Chem. Phys.* **2009**, *131*, 114304.
- (35) Greenman, L.; Ho, P. J.; Pabst, S.; Kamarchik, E.; Mazziotti, D. A.; Santra, R. Implementation of the time-dependent configuration-interaction singles method for atomic strong-field processes. *Phys. Rev. A* **2010**, *82*, 023406.
- (36) Tremblay, J. C.; Klinkusch, S.; Klamroth, T.; Saalfrank, P. Dissipative many-electron dynamics of ionizing systems. *J. Chem. Phys.* **2011**, *134*, 044311.
- (37) Krause, P.; Sonk, J. A.; Schlegel, H. B. Strong field ionization rates simulated with time-dependent configuration interaction and an absorbing potential. *J. Chem. Phys.* **2014**, *140*, 174113.
- (38) Krause, P.; Schlegel, H. B. Angle-Dependent Ionization of Hydrides AH_n Calculated by Time-Dependent Configuration Interaction with an Absorbing Potential. *J. Phys. Chem. A* **2015**, *119*, 10212–10220.
- (39) Worner, H. J.; Arrell, C. A.; Banerji, N.; Cannizzo, A.; Chergui, M.; Das, A. K.; Hamm, P.; Keller, U.; Kraus, P. M.; Liberatore, E.; et al. Charge migration and charge transfer in molecular systems. *Struct. Dyn.* **2017**, *4*, 061508.

- (40) Shu, Y. N.; Truhlar, D. G. Decoherence and its role in electronically nonadiabatic dynamics. *J. Chem. Theory Comput.* **2023**, 19, 380–395.
- (41) Meyer, H. D.; Manthe, U.; Cederbaum, L. S. The multiconfigurational time-dependent Hartree approach. *Chem. Phys. Lett.* **1990**, *165*, 73–78.
- (42) Beck, M. H.; Jackle, A.; Worth, G. A.; Meyer, H. D. The multiconfiguration time-dependent Hartree (MCTDH) method: a highly efficient algorithm for propagating wavepackets. *Phys. Rep.* **2000**, 324, 1–105.
- (43) Burghardt, I.; Meyer, H. D.; Cederbaum, L. S. Approaches to the approximate treatment of complex molecular systems by the multiconfiguration time-dependent Hartree method. *J. Chem. Phys.* **1999**, 111, 2927–2939.
- (44) Worth, G. A.; Burghardt, I. Full quantum mechanical molecular dynamics using Gaussian wavepackets. *Chem. Phys. Lett.* **2003**, *368*, 502–508.
- (45) Curchod, B. F. E.; Martinez, T. J. Ab initio nonadiabatic quantum molecular dynamics. *Chem. Rev.* **2018**, *118*, 3305–3336.
- (46) Shalashilin, D. V.; Child, M. S. Real time quantum propagation on a Monte Carlo trajectory guided grids of coupled coherent states: 26D simulation of pyrazine absorption spectrum. *J. Chem. Phys.* **2004**, *121*, 3563–3568
- (47) Saita, K.; Shalashilin, D. V. On-the-fly ab initio molecular dynamics with multiconfigurational Ehrenfest method. *J. Chem. Phys.* **2012**, *137*, 22A506.
- (48) Heller, E. J. Time-dependent approach to semiclassical dynamics. *J. Chem. Phys.* **1975**, *62*, 1544–1555.
- (49) Golubev, N. V.; Begusic, T.; Vanicek, J. On-the-fly ab initio semiclassical evaluation of electronic coherences in polyatomic molecules reveals a simple mechanism of decoherence. *Phys. Rev. Lett.* **2020**, *125*, 083001.
- (50) Scheidegger, A.; Vanicek, J.; Golubev, N. V. Search for long-lasting electronic coherence using on-the-fly ab initio semiclassical dynamics. *J. Chem. Phys.* **2022**, *156*, 034104.
- (51) Arnold, C.; Vendrell, O.; Santra, R. Electronic decoherence following photoionization: Full quantum-dynamical treatment of the influence of nuclear motion. *Phys. Rev. A* **2017**, *95*, 033425.
- (52) Arnold, C.; Lariviere-Loiselle, C.; Khalili, K.; Inhester, L.; Welsch, R.; Santra, R. Molecular electronic decoherence following attosecond photoionisation. *J. Phys. B: At. Mol. Opt. Phys.* **2020**, *53*, 164006.
- (53) Krause, P.; Schlegel, H. B. Angle-dependent ionization of small molecules by time-dependent configuration interaction and an absorbing potential. *J. Phys. Chem. Lett.* **2015**, *6*, 2140–2146.
- (54) Hoerner, P.; Schlegel, H. B. Angular dependence of strong field ionization of CH_3X (X = F, Cl, Br, or I) using time-dependent configuration interaction with an absorbing potential. *J. Phys. Chem. A* **2017**, *121*, 5940–5946.
- (55) Hoerner, P.; Schlegel, H. B. Angular dependence of ionization by circularly polarized light calculated with time-dependent configuration interaction with an absorbing potential. *J. Phys. Chem. A* **2017**, *121*, 1336–1343.
- (56) Hoerner, P.; Schlegel, H. B. Angular dependence of strong field ionization of haloacetylenes, HCCX (X = F, Cl, Br, I) using time-dependent configuration interaction with an absorbing potential. *J. Phys. Chem. C* **2018**, *122*, 13751–13757.
- (57) Winney, A. H.; Basnayake, G.; Debrah, D. A.; Lin, Y. F.; Lee, S. K.; Hoerner, P.; Liao, Q.; Schlegel, H. B.; Li, W. Disentangling strong-field multielectron dynamics with angular streaking. *J. Phys. Chem. Lett.* **2018**, 9, 2539–2545.
- (58) Lee, M. K.; Hoerner, P.; Li, W.; Schlegel, H. B. Effect of spin-orbit coupling on strong field ionization simulated with time-dependent configuration interaction. *J. Chem. Phys.* **2020**, *153*, 244109.
- (59) Lee, M. K.; Li, W.; Schlegel, H. B. Angular dependence of strong field sequential double ionization for neon and acetylene simulated with time-dependent configuration interaction using CIS and CISD-IP. *J. Chem. Phys.* **2020**, *152*, 064106.

- (60) Schlegel, H. B.; Hoerner, P.; Li, W. Ionization of HCCI neutral and cations by strong laser fields simulated with time dependent configuration interaction. *Front. Chem.* **2022**, *10*, 866137.
- (61) Golubeva, A. A.; Pieniazek, P. A.; Krylov, A. I. A new electronic structure method for doublet states: Configuration interaction in the space of ionized 1h and 2h1p determinants. *J. Chem. Phys.* **2009**, *130*, 124113.
- (62) Frisch, M. J.; Trucks, G. W.; Schlegel, H. B.; Scuseria, G. E.; Robb, M. A.; Cheeseman, J. R.; Scalmani, G.; Barone, V.; Petersson, G. A.; Nakatsuji, H.; et al. *Gaussian Development Version*, Revision J.02; Gaussian, Inc.: Wallingford CT, 2019.
- (63) Dunning, T. H. Gaussian basis sets for use in correlated molecular calculations. I. The atoms boron through neon and hydrogen. *J. Chem. Phys.* **1989**, *90*, 1007–1023.
- (64) Woon, D. E.; Dunning, T. H., Jr. Gaussian basis sets for use in correlated molecular calculations. III. The atoms aluminum through argon. *J. Chem. Phys.* **1993**, *98*, 1358–1371.
- (65) Peterson, K. A.; Shepler, B. C.; Figgen, D.; Stoll, H. On the spectroscopic and thermochemical properties of ClO, BrO, IO, and their anions. *J. Phys. Chem. A* **2006**, *110*, 13877–13883.
- (66) Peterson, K. A.; Figgen, D.; Goll, E.; Stoll, H.; Dolg, M. Systematically convergent basis sets with relativistic pseudopotentials. II. Small-core pseudopotentials and correlation consistent basis sets for the post-d group 16–18 elements. *J. Chem. Phys.* **2003**, *119*, 11113–11123.
- (67) Mathematica, version 12.0; software for technical computation; Wolfram Research, Inc.: Champaign, IL, 2019.
- (68) Allan, M.; Klosterjensen, E.; Maier, J. P. Emission-spectra of Cl-C=C-H $^+$,Br-C=C-H $^+$ and I-C=C-H $^+$ radical cations A- $^2\Pi$ X- $^2\Pi$ band systems and decay of A- $^2\Pi$ states. *J. Chem. Soc., Faraday Trans.* **1977**, 73, 1406–1416.
- (69) Maier, J. P.; Ochsner, M. The A- $^2\Pi_{3/2}$ -X- $^2\Pi_{3/2}$ laser-excitation spectra of iodoacetylene and deuteroiodoacetylene cations. *J. Chem. Soc., Faraday Trans.* 2 **1985**, *81*, 1587–1598.
- (70) Fulara, J.; Klapstein, D.; Kuhn, R.; Maier, J. P. Emission-spectra of supersonically cooled haloacetylene cations $XC=C-H(D)^+$, X=Br, I. J. Phys. Chem. **1986**, 90, 2061–2067.
- (71) Vester, J.; Despre, V.; Kuleff, A. I. The role of symmetric vibrational modes in the decoherence of correlation-driven charge migration. *J. Chem. Phys.* **2023**, *158*, 104305.
- (72) Hassan, M. T.; Luu, T. T.; Moulet, A.; Raskazovskaya, O.; Zhokhov, P.; Garg, M.; Karpowicz, N.; Zheltikov, A. M.; Pervak, V.; Krausz, F.; et al. Optical attosecond pulses and tracking the nonlinear response of bound electrons. *Nature* **2016**, *530*, 66–70.
- (73) Liang, H. K.; Krogen, P.; Wang, Z.; Park, H.; Kroh, T.; Zawilski, K.; Schunemann, P.; Moses, J.; DiMauro, L. F.; Kartner, F. X.; et al. High-energy mid-infrared sub-cycle pulse synthesis from a parametric amplifier. *Nat. Commun.* **2017**, *8*, 141.
- (74) Timmers, H.; Kobayashi, Y.; Chang, K. F.; Reduzzi, M.; Neumark, D. M.; Leone, S. R. Generating high-contrast, near single-cycle waveforms with third-order dispersion compensation. *Opt. Lett.* **2017**, *42*, 811–814.